JOURNAL OF AIRCRAFT
Vol. 40, No. 2, March–April 2003

FENSAP-ICE's Three-Dimensional In-Flight Ice Accretion Module: ICE3D

Héloïse Beaugendre,* François Morency,† and Wagdi G. Habashi‡
McGill University, Montreal, Quebec H3A 2S6, Canada

Two-dimensional and quasi-three-dimensional in-flight ice accretion simulation codes have been increasingly used by the aerospace industry in the last two decades as an aid to the certification process. Such codes predict two-dimensional sectional ice shapes, which are then manufactured from a light material and attached as disposable profiles on test aircraft to investigate them for stability under icing encounters. Although efficient for calculating ice shapes on simple geometries, current codes encounter major difficulties or simply cannot simulate ice shapes on truly three-dimensional geometries such as nonaxisymetric nacelles, high-lift wings, engine intakes, or systems that combine external and internal flows. Modern computational fluid dynamics approaches may not encounter or engender these difficulties, and FENSAP-ICE is a combination of four modules forming a complete and generic in-flight icing simulation system, built in a way to solve successively impingement, ice accretion, heat loads, and performance degradation via new mathematical models based on the Navier–Stokes equations for the flow and Navier–Stokes-like partial differential equations for the three other processes. The set of equations describing FENSAP-ICE's airflow solver, FENSAP, its impingement module, DROP3D, and its accretion module, ICE3D, are presented. Also a validation roadmap of ICE3D, for both two- and three-dimensional geometries, is presented.

Nomenclature

C_{ice}	=	specific heat for ice
C_w	=	specific heat for water
c_f	=	friction coefficient
c_p	=	specific heat at constant pressure
d, r_d	=	droplet diameter, radius
Fr	=	Froude number, $[U_\infty/\sqrt{(L\boldsymbol{g}_0)}]$
$\boldsymbol{g}$	=	gravity vector
$\boldsymbol{g}_0$	=	magnitude of the gravity vector
h	=	heat transfer coefficient
h_f	=	film thickness
K	=	droplet inertia parameter, $(\rho_w d^2 U_\infty/18L\mu_w)$
k_s	=	equivalent sand grain roughness diameter
L	=	characteristic length
L_{evap}	=	latent heat of evaporation
L_{fusion}	=	latent heat of fusion at 0°C
L_{subl}	=	latent heat of sublimation
$\dot{m}_{\text{evap}}$	=	instantaneous mass of evaporation
$\dot{m}_{\text{ice}}$	=	instantaneous mass of ice accretion
$\boldsymbol{n}$	=	vector normal to the wall
p	=	pressure
$\dot{Q}_h$	=	convective heat flux
Re_d	=	droplet Reynolds number $[dU_\infty(\boldsymbol{u}_a - \boldsymbol{u}_d)/\nu]$
s	=	curvilinear distance from stagnation point
T	=	temperature at wall/air/liquid-water/ice interface, K
$\tilde{T}$	=	temperature at wall/air/liquid-water/ice interface, °C
$\tilde{T}_{d,\infty}$	=	droplets temperature at infinity, °C
T_∞	=	temperature at infinity, K
t	=	time
U_∞	=	velocity at infinity
$\boldsymbol{u}, \bar{\boldsymbol{u}}$	=	film velocity vector and mean film velocity across the thickness
u_a	=	air velocity
$\boldsymbol{u}_d$	=	droplets velocity
u_e	=	velocity at the edge of the boundary layer
X	=	rotor blade tip chordwise direction
$\boldsymbol{x}$	=	coordinate along the wall, (x_1, x_2)
Y	=	rotor blade tip spanwise direction
y	=	coordinate normal to the wall
Z	=	normal direction to the plane (X, Y)
α	=	water volume fraction
β	=	collection efficiency
ε	=	solid emissivity
μ	=	laminar dynamic viscosity
μ_w	=	dynamic viscosity of water
ν	=	laminar kinematic viscosity
$\tilde{\nu}$	=	dimensionless turbulent viscosity
ρ_a	=	air density
ρ_w	=	water density
σ	=	Boltzman constant
τ_{wall}	=	air wall shear stress tensor

Presented as Paper 2002-385 at the AIAA 40th Aerospace Sciences and Exhibit Conference, Reno, NV, 14 January 2002; received 21 February 2002; revision received 21 October 2002; accepted for publication 21 October 2002.

*Ph.D. Candidate, Computational Fluid Dynamics Laboratory, 688 Sherbrooke Street West.

†Research Associate, Computational Fluid Dynamics Laboratory, 688 Sherbrooke Street West.

‡Professor and Director, Computational Fluid Dynamics Laboratory, 688 Sherbrooke Street West. Associate Fellow AIAA.

Introduction

BECAUSE not all certification conditions can be ice tunnel tested, flight tested, tank tested, or encountered in natural icing testing, only analytical methods make it possible to explore, safely, the entire icing envelope. The icing community traditionally used analytical methods to calculate impingement limits and predict ice shapes to be attached to aircraft for flight testing. Such methods are based on either two-dimensional or quasi-three-dimensional inviscid panel (incompressible potential[1]) flow codes to compute the airflow solution, on Lagrangian tracking techniques for droplet impingement calculations, and on a one-dimensional mass and heat transfer balance at the surface to predict ice shapes. Computational fluid dynamics (CFD) technologies can overcome some of the limitations of these analytical approaches and open the way to couple aerodynamics and icing to assess the stability and control of iced aircraft or to build CFD databases for in-flight icing.

The approach suggested here views icing accretion simulation as the solution of 1) the compressible turbulent Navier–Stokes

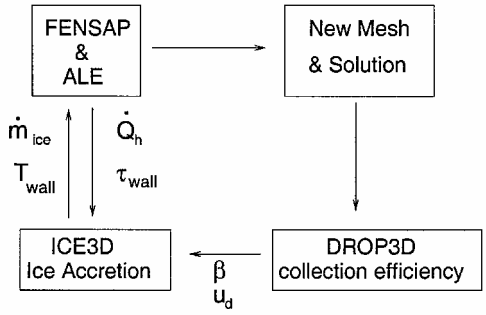

Fig. 1 Module interactions within FENSAP-ICE.

equations (by any CFD code, here with FENSAP[2]); 2) the computation of the collection efficiency by an Eulerian method (here with DROP3D[3]); 3) the solution of three-dimensional, that is, two- and-one-half-dimensional, following the aerodynamic surface, mass balance and heat transfer at surface, using partial differential equations (PDE), for prediction of ice accretion shapes (here with ICE3D[4]); and 4) a conjugate heat transfer problem, in the presence of an antiicing heat flux across the wing skin (for example, with the use of CHT3D[5]).

All four codes are PDE based. Only icing calculations will be presented in this paper. As shown in Fig. 1, the first three modules are set in an interactive loop. Each system of PDEs (airflow/impingement/accretion) is solved independently, with selected variables passed between modules when required. FENSAP and DROP3D use a weak Galerkin finite element method (FEM), on structured, on unstructured, and on hybrid meshes. In the ice accretion module, ICE3D, a finite volume method (FVM) is found more suitable for such two- and- one-half-dimensional formulations. In FENSAP-ICE, the distortion of the solid surfaces caused by ice growth is transparently accounted for by an arbitrary Lagrangian Eulerian (ALE) scheme embedded in the flow solver.

The first part of this paper will briefly recall the governing equations of each of the three modules and will show some two-dimensional validations of the entire FENSAP-ICE system. The focus of the work presented here had been to compare numerical three-dimensional ice accretion with experimental results, which are rare. The results of Hedde and Guffond[6] were chosen, and from their published information, clearly given as being based on known NACA 13106 profiles, we were able to reconstruct a complete three-dimensional geometry with which we carried out the calculations. However, the two-dimensional cuts of the geometry they show have small waves that could be caused by a poor printing quality, and moreover, the clean profiles turned out not to be from a NACA 13106. After some talks with Eurocopter engineers, it became clear that the exact geometry was and will remain confidential. The geometry may have been based on a NACA 13106 profile, but the final profiles are quite different from that base shape. As a consequence, the three-dimensional results presented in the last section will be compared only qualitatively to experiments. It is hoped that with the advent of three-dimensional simulation codes, more experimental data will be generated for validation.

FENSAP-ICE's Modules Description

Accurate turbulent heat fluxes are essential to the simulation of ice accretion. Our current airflow solver, FENSAP, can be used with a one-equation turbulence model[7] or two-equation models (low Reynolds and high Reynolds k–ε and k–ω). Currently, the FENSAP-ICE system can use a structured, unstructured, or hybrid mesh for all of the modules composing its interactive chain, which means a one-time mesh generation effort.

Each part of the modular system will be briefly described in terms of the equations and numerical method used.

FENSAP

In the Spalart–Allmaras[7] model, the transport equation for the dimensionless turbulent viscosity $\tilde{\nu}$ is

$$\frac{\mathrm{D}\tilde{\nu}}{\mathrm{D}t} = cb_1[1 - f_{t2}]\tilde{S}\tilde{\nu} + \frac{1}{\sigma Re_\infty}\left\{\nabla\cdot[(\nu+\tilde{\nu})\nabla\tilde{\nu}] + cb_2(\nabla\tilde{\nu})^2\right\} - \frac{1}{Re_\infty}\left[c_{w1}f_w - \frac{cb_1}{\kappa^2}f_{t2}\right]\left[\frac{\tilde{\nu}}{d}\right]^2 + Re_\infty f_{t1}(\Delta U)^2 \quad (1)$$

where d is the distance from the wall, $\tilde{S}$ is the vorticity, cb_1, cb_2, c_{w1}, κ, and σ are the closure coefficients, and f_w is the closure function. This equation has been shown to be particularly attractive for unstructured meshes with one or more types of element.

The tripping functions, f_{t1} and f_{t2}, allow user control over the transition from laminar to turbulent flow. The extension for rough-wall treatment,[8] essential in icing simulation, has been included in the model. For a roughness coefficient k_s, the conventional Nikuradse sandgrain roughness, the distance from the wall is increased as follows:

$$d_s = d + 0.03k_s \quad (2)$$

This extension requires nonzero wall values of $\tilde{\nu}$ and a mixed wall boundary condition expressed by

$$\frac{\partial\tilde{\nu}}{\partial \boldsymbol{n}} = \frac{\tilde{\nu}}{d}$$

Spatial discretization is carried out by the FEM, and the equation is linearized by a Newton method. To advance the solution in time, an implicit Gear scheme is used, along with a generalised minimal residual procedure to solve iteratively the resulting matrix system. Heat fluxes at the wall are calculated via a consistent FEM approach.[9]

DROP3D

DROP3D is a fully three-dimensional Eulerian approach for airflows containing water droplets. Suitable variables (water volume fraction and droplet velocity) are computed at the same nodes of the discrete domain where the airflow variables are known, so that no particles have to be tracked through the mesh as in a Lagrangian approach. Some of the advantages of this physical approach are the quality of the solution, the accuracy of the impingement limits, and the determination of shadow zones (no impingement) for probes or detectors placing.

The Eulerian model used for the impingement calculations has been introduced by Bourgault et al.[3] It is a two-fluid model consisting of the Euler or Navier–Stokes equations for air, augmented by the following droplet-related continuity and momentum equations:

$$\frac{\partial\alpha}{\partial t} + \nabla\cdot(\alpha\boldsymbol{u}_d) = 0 \quad (3)$$

$$\frac{\partial\boldsymbol{u}_d}{\partial t} + \boldsymbol{u}_d\cdot\nabla\boldsymbol{u}_d = \frac{C_D Re_d}{24K}(\boldsymbol{u}_a - \boldsymbol{u}_d) + \left(1 - \frac{\rho_a}{\rho_w}\right)\frac{1}{Fr^2}\boldsymbol{g} \quad (4)$$

The first right-hand-side term of Eq. (4) is the air drag force on the droplets, and the second represents buoyancy and gravity forces. The nondimensional air velocity $\boldsymbol{u}_a$ is obtained using a Navier–Stokes or Euler solver, here FENSAP.

An empirical equation gives the drag coefficient for spherical droplets used in Eq. (4),[10]

$$C_D = (24/Re_d)\left(1 + 0.15Re_d^{0.687}\right) \quad \text{for} \quad Re_d \le 1300$$
$$C_D = 0.4 \quad \text{for} \quad Re_d > 1300 \quad (5)$$

The droplets' velocity, as well as the liquid water content, is imposed at the freestream. The droplet velocity is set to zero on all walls at the beginning of the calculations. No boundary conditions are needed at the exit, due to the hyperbolicity of the equation system. A finite element method is used to discretize the equations, with a streamline upwinding Petrov–Galerkin stabilization term (see Ref. 11) added.

ICE3D

Once the frictional forces and the heat fluxes are determined from the viscous-turbulent airflow solution (here, FENSAP) and the mass rate of water caught is known from the impingement module (here, DROP3D), the ice accretion can be assessed by ICE3D. ICE3D's physical model essentially consists of converting the classical Messinger model[12] into a PDE system of conservation equations,[13] thus, allowing a natural extension from two to three dimensions, as well as a fine grain solution.

Mathematical Model and Numerical Approach

The velocity $\boldsymbol{u}$ of the water in the film is a function of coordinates $\boldsymbol{x} = (x_1, x_2)$ on the surface and y normal to the surface. For very thin films, the terms of order higher than one in the velocity profile are negligible. In icing or antiicing simulations, film thickness is seldom above 10 μm (Ref. 14). Hence, a simplifying assumption consists of taking a linear profile for $\boldsymbol{u}(\boldsymbol{x}, y)$, with a zero velocity imposed at the wall, that is,

$$\boldsymbol{u}(\boldsymbol{x}, y) = \left(\frac{\tau_{\text{wall}}}{\mu_w} - \frac{h_f}{\mu_w} \frac{\mathrm{d}p}{\mathrm{d}s} \right) y(\boldsymbol{x}) \tag{6}$$

where τ_{wall}, the shear stress from the air, is the main driving force for the water film and the pressure force is negligible except close to the stagnation point. Take, for example, the dimensionless pressure gradient at a stagnation point in two dimensions defined by[15]

$$-\frac{s}{\rho u_e^2} \frac{\mathrm{d}p}{\mathrm{d}s} = 1 \tag{7}$$

where u_e is the velocity just outside the boundary layer and s the distance from stagnation point. Pressure forces are negligible if

$$\tau_{\text{wall}} \gg h_f \frac{\mathrm{d}p}{\mathrm{d}s} \tag{8}$$

When the definition of the friction coefficient and Eq. (7) are used, Eq. (8) becomes

$$0.5 c_f \gg h_f / s$$

For a small water film thickness h_f, the pressure gradient could have an effect only very close to the stagnation point or near a separation point. With similar arguments, gravity force can be shown to be negligible except in the vicinity of a stagnation point or a separation point.[16]

By the average along the thickness of the film, a mean velocity is obtained:

$$\bar{\boldsymbol{u}}(\boldsymbol{x}, y) = \frac{1}{h_f} \int_0^{h_f} \boldsymbol{u}(\boldsymbol{x}, y)\, \mathrm{d}y = \frac{h_f}{2\mu_w} \tau_{\text{wall}}(\boldsymbol{x}) \tag{9}$$

Because the water film is very thin, temperature changes in the direction normal to the wall are small. Thus, a constant average temperature through the water film is used.

The resulting system of partial differential equations is as follows.

Mass conservation:

$$\rho_w \left[\frac{\partial h_f}{\partial t} + \operatorname{div}(\bar{\boldsymbol{u}} h_f) \right] = U_\infty \text{LWC} \beta - \dot{m}_{\text{evap}} - \dot{m}_{\text{ice}} \tag{10}$$

where the three terms on the right-hand-side correspond to the mass transfer by water droplet impingement (source for the film), the evaporation, and the ice accretion (sinks for the film), respectively.

Energy conservation:

$$\rho_w \left[\frac{\partial h_f C_w \tilde{T}}{\partial t} + \operatorname{div}(\bar{\boldsymbol{u}} h_f C_w \tilde{T}) \right] = \left[C_w \tilde{T}_{d,\infty} + \frac{\|\boldsymbol{u}_d\|^2}{2} \right] \times U_\infty \text{LWC} \beta - 0.5 (L_{\text{evap}} + L_{\text{subl}}) \dot{m}_{\text{evap}} + (L_{\text{fusion}} - C_{\text{ice}} \tilde{T}) \dot{m}_{\text{ice}} + \varepsilon \sigma \left(T_\infty^4 - T^4 \right) + \dot{Q}_h \tag{11}$$

where the first three terms on the right-hand-side model correspond, to the heat transfer caused by the supercooled water droplets impingement, the evaporation, and the ice accretion, respectively. The last two terms represent the radiative and convective heat transfer. Following an idea of Hedde,[16] half of the water is considered liquid and the other half solid when evaporation occurs. The heat losses by radiation are included, although they are important only in antiicing simulation. Conduction through the metal skin is neglected, based on the fact that ice acts somewhat as an insulator.[17]

The convective heat transfer provided by the flow solver is converted into a heat transfer coefficient, before the ice accretion calculations:

$$h = \dot{Q}_h / (T - T_\infty) \tag{12}$$

The heat transfer coefficient depends only weakly on the surface temperature distribution along the airfoil, but will change depending on the boundary-layer thickness. Therefore, between each call to the flow solver, Eq. (11) uses a fixed value for $h(\boldsymbol{x})$ to obtain a convective heat flux that depends on surface temperature T.

The coefficients ρ_w, C_w, C_{ice}, L_{evap}, L_{subl}, L_{fusion}, and σ represent physical properties, whereas $T_{d,\infty}$, U_∞, liquid water content (LWC), and T_∞ are airflow and droplet parameters specified by the user. The ambient icing conditions completely determine those values. The tilde over T, that is, $\tilde{T}$, indicates the temperature is in degrees Celsius, otherwise temperature is in degrees Kelvin.

The Eulerian droplet module provides local values for the collection efficiency β and the droplet impact velocity $\boldsymbol{u}_d$. The flow solver provides the local wall shear stress τ_{wall} and the convective heat flux $\dot{Q}_h$. The evaporative mass flux is recovered from the convective heat flux using a parametric model.[18] There remain three unknowns: the film thickness h_f, the equilibrium temperature $\tilde{T}$ within the air/water film/ice/wall interface, and the instantaneous mass accumulation of ice $\dot{m}_{\text{ice}}$. Compatibility relations are needed to close the system, and one way to write them is the following:

$$h_f \geq 0 \tag{13}$$

$$\dot{m}_{\text{ice}} \geq 0 \tag{14}$$

$$h_f \tilde{T} \geq 0 \tag{15}$$

$$\dot{m}_{\text{ice}} \tilde{T} \leq 0 \tag{16}$$

The discretization of the equations is via a FVM. The hull of the three-dimensional mesh at the air-structure/ice shape interface is called the surface mesh. From the surface mesh, a dual surface mesh is obtained by connecting the baricenters of the surface mesh cells to the midedges of the cells. The unknowns are computed at the center of each cell, thus, corresponding one-to-one to the nodes of the finite element grid used for the air and droplet solutions.

Comparison with Two-Dimensional Experimental and Numerical Results

ICE3D has been compared to numerical results obtained with LEWICE and experimental results from the NASA John H. Glenn Research Center at Lewis Field icing research tunnel (IRT).[19] All calculations are done on three-dimensional meshes of one element thickness in the spanwise direction. A consensus about the comparison of two ice shapes is difficult to obtain in icing. The focus can be on different criteria such as the limit of impact, the ice thickness, the location and angle of a possible horn, etc. As a consequence, the comparisons remain subjective most of the time, but conservative enough to meet best aircraft safety.

In the first comparison, ice is accreted 7 min on a NACA 0012 airfoil at an angle of attack of 3.5 deg. The ambient icing conditions, which should be close to a rime ice accretion, are given in Table 1 and correspond to LEWICE run 404. The first 5 min of accretion are calculated in five, 1-min time steps and compared to LEWICE solution in Fig. 2. The first minute of ice accretion is almost identical for ICE3D and LEWICE. The limits of impact are the same, and the ice thickness coincides almost everywhere. The location and angle of the upper bump match in the two numerical solutions. Notice

Table 1 Ambient conditions for run 404

Parameter	Value
T_∞	256.49 K
P_∞	90.76 kPa
U_∞	102.8 m · s^{-1}
Angle of attack	3.5 deg
MVD	20 μm
LWC	0.55 g/m^3
Re_∞	4.14×10^6

Table 2 Ambient conditions for run 308

Parameter	Value
T_∞	262.04 K
P_∞	90.76 kPa
U_∞	102.8 m · s^{-1}
Angle of attack	3.5 deg
MVD	20 μm
LWC	1.0 g/m^3
Re_∞	4.14×10^6

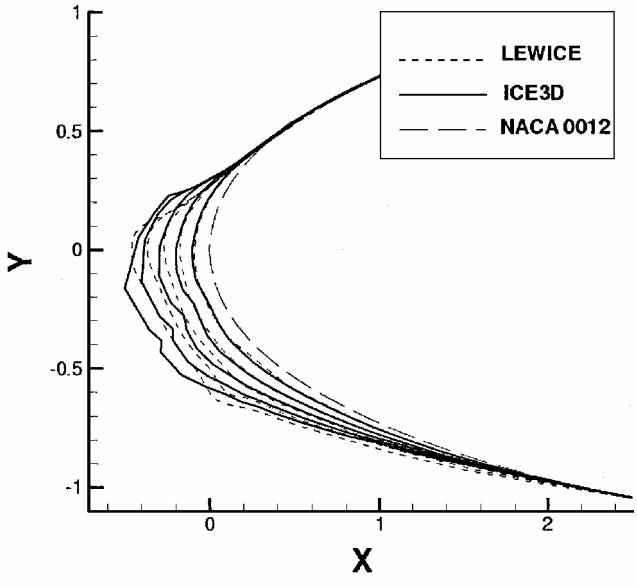

Fig. 2 Run 404 [NASA CD-ROM][19] comparison between ICE3D and LEWICE after 1, 2, 3, 4, and 5 min of ice accretion.

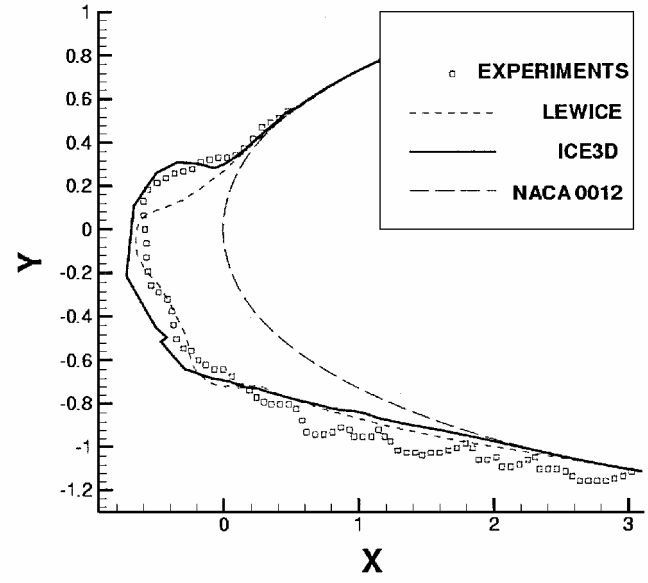

Fig. 3 Run 404 [NASA CD-ROM][19] comparison between ICE3D, LEWICE, and IRT experimental ice shape.

that ICE3D slightly overpredicts the ice thickness on the top bump and just below stagnation point. This can be explained by a larger amount of runback predicted by LEWICE. Naturally, the differences magnify after each update of the airflow and droplet solutions. Note that ICE3D does not use a filter to smooth the ice shape after each time step, contrasted to other codes. Large and complex ice shapes constitute a constraint for the automatic mesh movement using ALE inside the flow solver. At the end of each run, ICE3D returns the modified skin mesh taking into account the ice thickness. If the ALE method fails, it is then possible to use this information to construct a new mesh and continue the simulation. The ALE constraint can be eventually removed by coupling mesh adaptation tools inside the flow solver.

The behavior observed during the first time steps is still present in the final ice shape after 7 min of accretion. Figure 3 shows the final ice shape computed by LEWICE and ICE3D, compared to the experimental ice shape obtained in the IRT. The limits of impact are identical for LEWICE and ICE3D and match the experiments on the suction side of the airfoil but are underpredicted by both codes on the pressure side of the airfoil. Globally LEWICE predicts a larger amount of water runback than ICE3D. As a result, ICE3D's ice shape is thicker and closer to the experimental ice shape than LEWICE on the upper part of the airfoil. The smaller amount of runback predicted by ICE3D also results in a slightly lower ice thickness on the pressure side, where LEWICE solution is closer to the experiments.

In the second comparison, ice is accreted on a NACA 0012 airfoil at an angle of attack of 3.5 deg for 231 s. The ambient conditions, closer to glaze ice conditions, are summarized in Table 2 and correspond to LEWICE run 308. Figure 4 shows the comparison between LEWICE and ICE3D numerical solutions after 47.58 and 95.16 s of accretion. At 47.58 s of accretion, ICE3D and LEWICE solutions are identical: same ice thickness and limits of impact for both codes. At 95.16 s of accretion, LEWICE and ICE3D solutions remain very close to each other, LEWICE predicting a slightly bigger amount

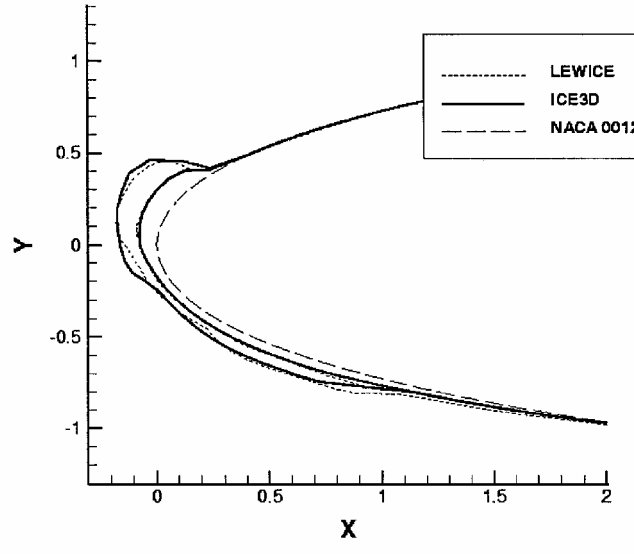

Fig. 4 Run 308 [NASA CD-ROM][19] comparison between ICE3D and LEWICE after 47.58 and 95.16 s of ice accretion.

of runback than ICE3D. Both codes predict the formation of a horn on the upper part of the NACA 0012 airfoil, with the same angle and ice thickness. After 95.16 s of accretion, the horn predicted by ICE3D induces a separation in the flow solution. Contrary to LEWICE, which may not be able to predict separation with only a viscous/inviscid interaction, ICE3D's convective heat transfer coefficient and shear stress decrease suddenly in the separation area. As a consequence the horn predicted by FENSAP-ICE is magnified by the separation as in Fig. 5. ICE3D's final ice shape differs from LEWICE's, but both qualitatively agree with the experimental ice shape.

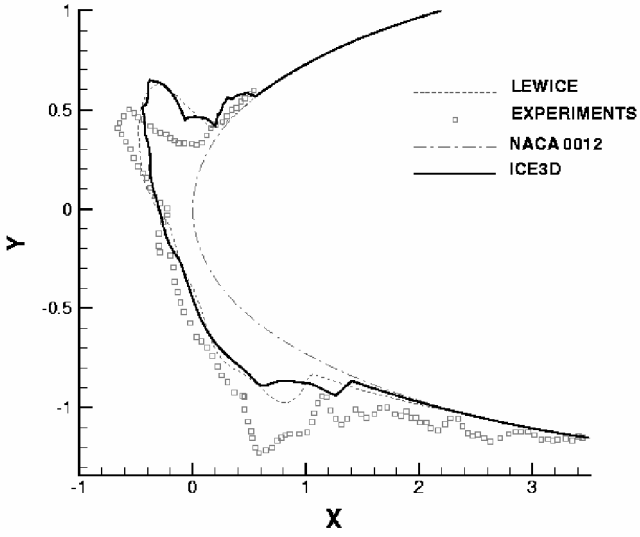

Fig. 5 Run 308 [NASA CD-ROM][19] comparison between ICE3D, LEWICE, and IRT experimental ice shape.

Three-Dimensional Helicopter Rotor Blade Tip Results

A three-dimensional helicopter rotor tip geometry is succinctly described in Ref. 6 as follows:

> . . .from the base to the top along the span, the chord varies from 0.6 to 0.2 m, the leading-edge sweep angle starts at 0 and ends at 60 deg. The trailing edge is perpendicular to the flow and is lightly spun so that the incidence angle at the top is 0.74 deg less than at the base. The span is 0.48 m. The rotor blade tip is built from a NACA 13106 airfoil.

The CAD of the geometry was produced with the ICEM DDN software. The one-equation Spalart–Allmaras[7] model was used for turbulence modeling, and mesh adaptation was carried out with OptiMesh,[20] an automatic anisotropic (highly directional and highly stretched) mesh adaptation code.

Airflow Solution and Mesh Adaptation

The conditions for the simulation are shown in Table 3. To improve the quality of the flow solution, three mesh adaptation cycles were carried out with OptiMesh. The OptiMesh algorithm utilizes mesh movement, edge refinement, coarsening, and swapping to yield automatically a nearly optimal anisotropic, that is, highly directional and stretched, adapted grid. Figures 6–10 show two-dimensional cuts of the three-dimensional grid after each mesh adaptation cycle. The initial mesh contains 221,800 nodes and 1,118,131 elements, and the last adapted one has 467,705 nodes and 2,546,857 elements.

The equivalent sandgrain roughness used is obtained using the equation[17] and corresponds to 0.269 mm in this case:

$$k_s = \left[\frac{k_{slc}}{k_{slc})_{\text{base}}}\right]_{Y_\infty} \left[\frac{k_{slc}}{k_{slc})_{\text{base}}}\right]_{\text{LWC}} \left[\frac{k_{slc}}{k_{slc})_{\text{base}}}\right]_{T_s} k_{slc})_{\text{base}} c \qquad (17)$$

To help the discussion of the results, two-dimensional (X, Z) cuts at four different spanwise locations are presented. The cuts are referred to as station 1 ($Y = 0.09$ m), station 2 ($Y = 0.25$ m), station 3 ($Y = 0.30$ m), and station 4 ($Y = 0.45$ m). The origin of the coordinate system is at the root of the wing at the leading edge. The Y axis is normal in the spanwise direction, and the X axis is in the chordwise direction.

As presented in Fig. 11, the finite blade modeled in this paper engenders three-dimensional aerodynamic effects, first with the creation of a local aerodynamic angle of attack different from the freestream and, second, with the creation of a tip vortex at the blade extremity. Because of a negative twist angle and a high angle of attack, the numerical solution shows a separation and a small sweep angle in that region. All aerodynamic variables are affected by this flow pattern. The distributions of turbulent viscosity are presented in Fig. 12.

Table 3 Ambient conditions for helicopter rotor blade tip simulation

Parameter	Value
T_∞	−30.5°C
P_∞	45.6 kPa
Mach	0.52
Angle of attack	9.5 deg
MVD	20 μm
LWC	1 g/m^3
Time	91 s

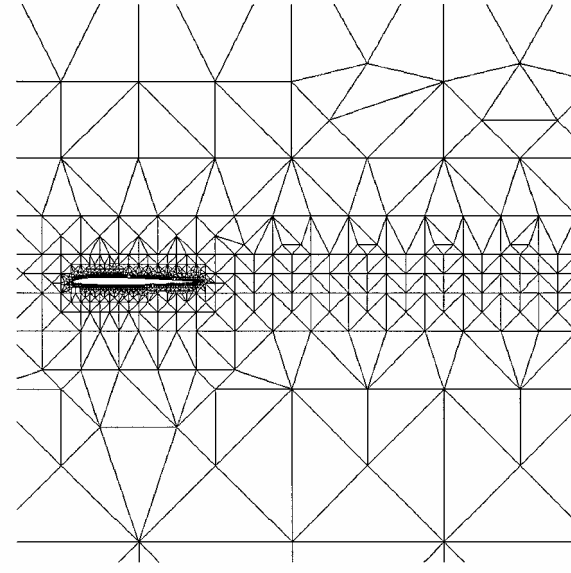

Fig. 6 Three-dimensional rotor blade tip, initial mesh.

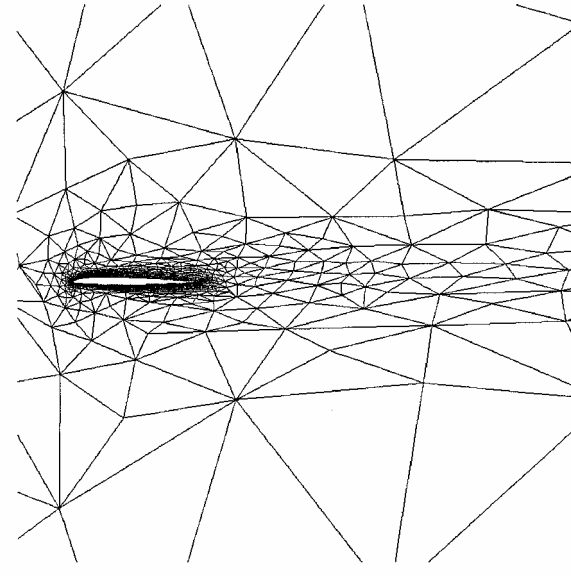

Fig. 7 Three-dimensional rotor blade tip, first OptiMesh adaptation cycle.

Figure 13 shows the convective heat transfer coefficient for stations 1–4. The heat transfer coefficient curves are quite similar along the blade, except close to the tip where the separation decreases the airspeed and, hence, the heat transfer coefficient.

Collection Efficiency Distribution

The droplet solution has also been computed by DROP3D on the adapted grid, using the FENSAP adapted airflow solution. Figure 14 presents the collection efficiency distribution on the blade, with

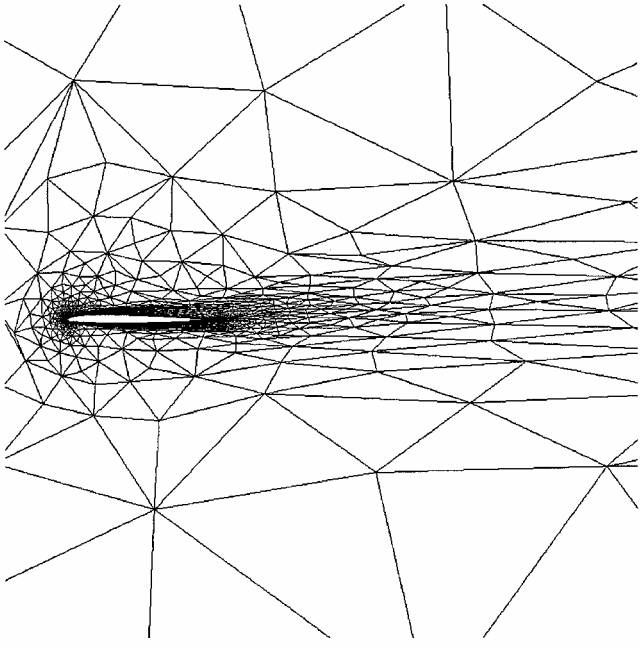

Fig. 8 Three-dimensional rotor blade tip, second OptiMesh adaptation cycle.

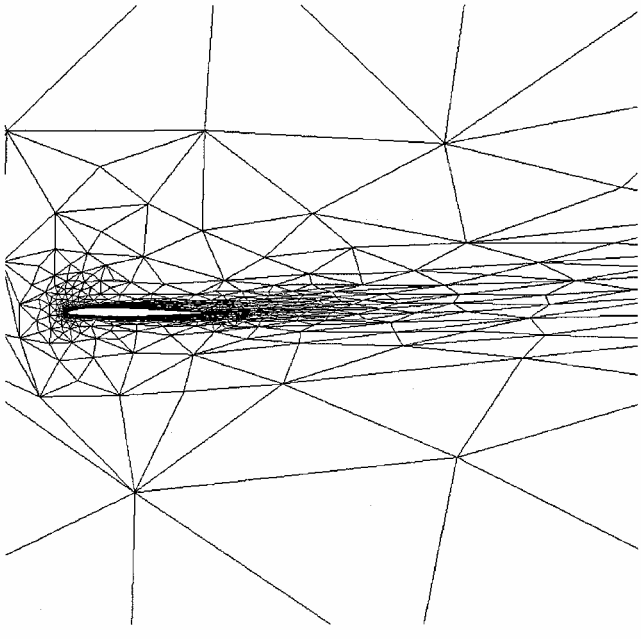

Fig. 9 Three-dimensional rotor blade tip, third OptiMesh adaptation cycle.

water volume fraction contours. The water volume fraction increases in the recirculation zone induced by the tip vortex.

The maximum of the collection efficiency increases with the length of the chord due to the scale factor from one spanwise airfoil section to another.

In Figs. 15 and 16, the airfoil section corresponding to each station is presented in nondimensional units, using the chord length, to make comparison easier. Usually the β curves are created using curvilinear coordinates with the origin located at the stagnation point. Finding the stagnation line in three dimensions is, however, not always an easy task, and we choose to represent the curves in the inner coordinates (X, Y, Z) even if it becomes a little more difficult to find the part of the curve corresponding to the upper part of the wing and the one corresponding to the lower part. The limit of impingement on the lower side of the blade extends farther back, closer to the tip (Fig. 15). On the other hand, the impingement limit

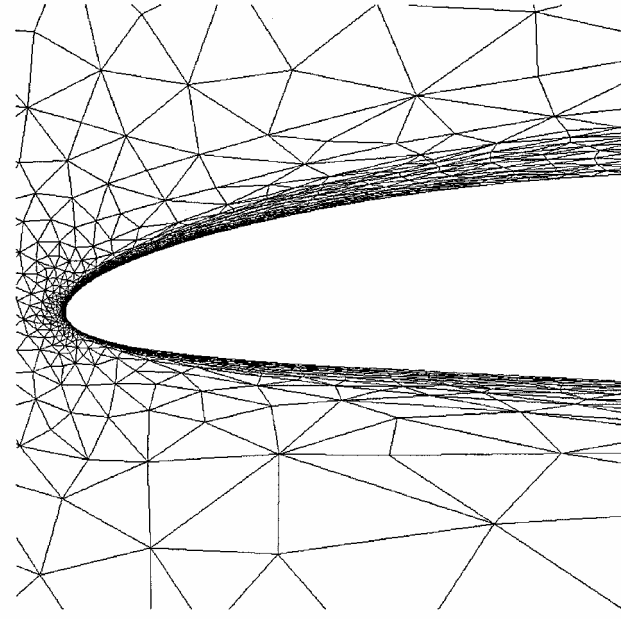

Fig. 10 Three-dimensional rotor blade tip, zoom on leading edge at adaptation 3.

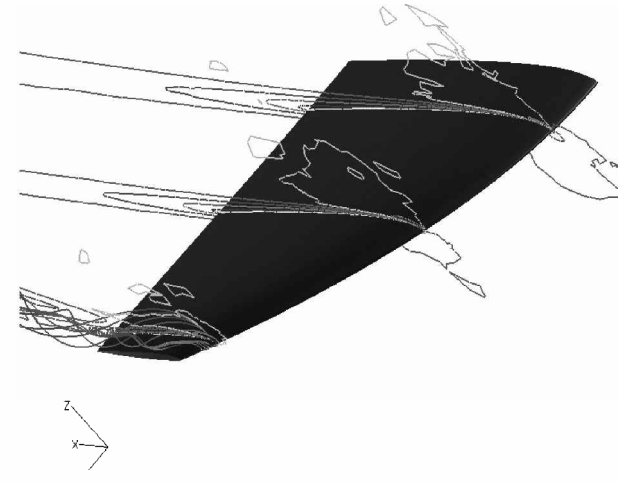

Fig. 11 Three-dimensional rotor blade tip, turbulent airflow solution, Mach number contours, and streamlines at the tip.

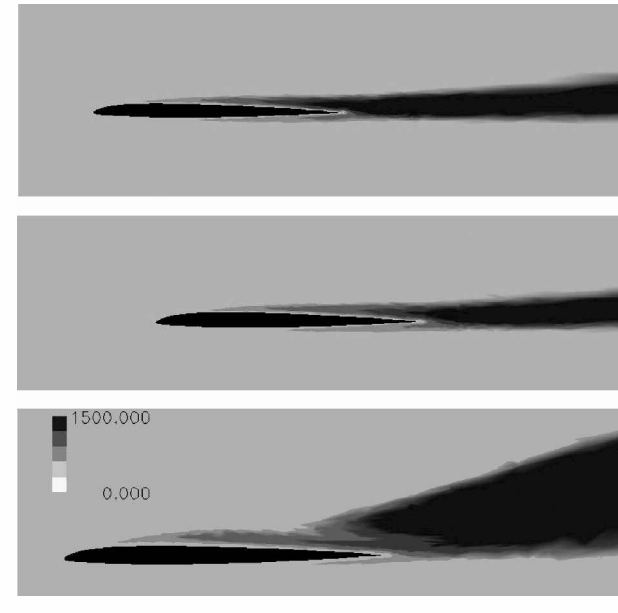

Fig. 12 Turbulent viscosity distribution at stations 1, 2, and 4.

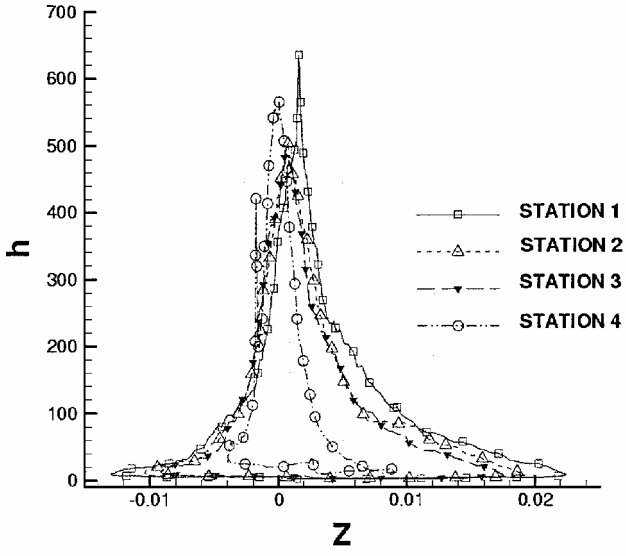

Fig. 13 Two-dimensional cuts of the convective heat transfer coefficient, in watts per square meter degrees Kelvin.

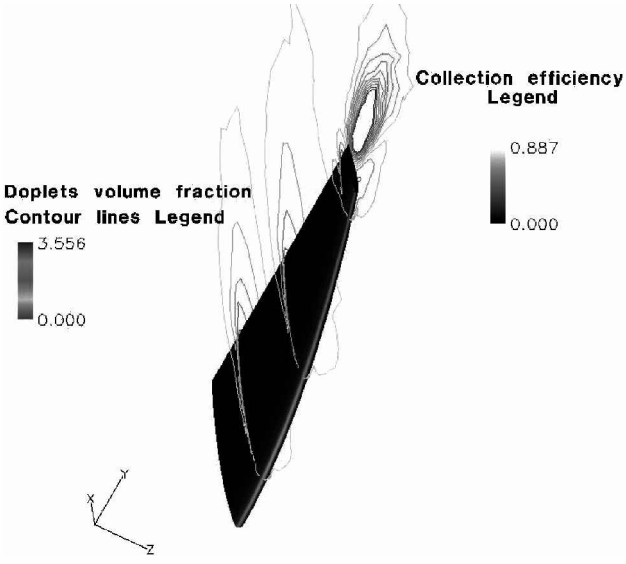

Fig. 14 Collection efficiency distribution on the wing and liquid water volume fraction contours for stations 1, 2, and 4.

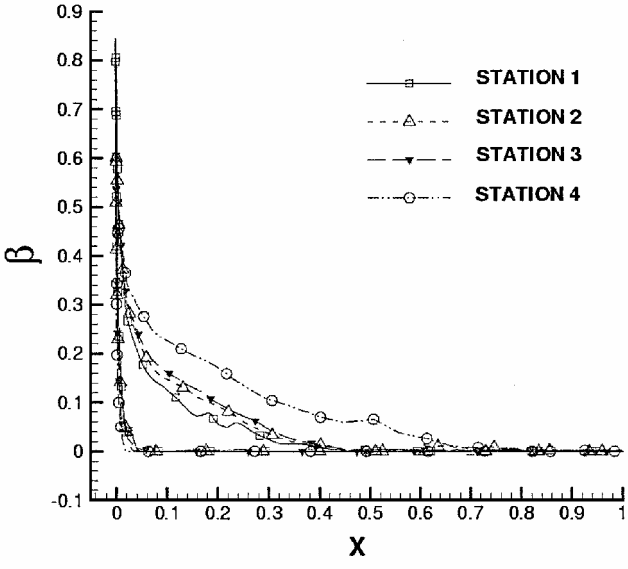

Fig. 15 Two-dimensional cuts of the collection efficiency for stations 1–4 along the nondimensional X axis, the chord direction.

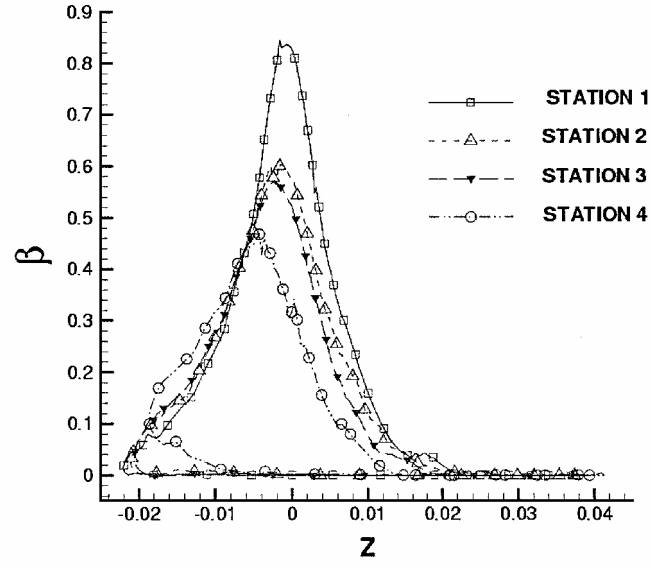

Fig. 16 Two-dimensional cuts of the collection efficiency for stations 1–4 along the Z axis.

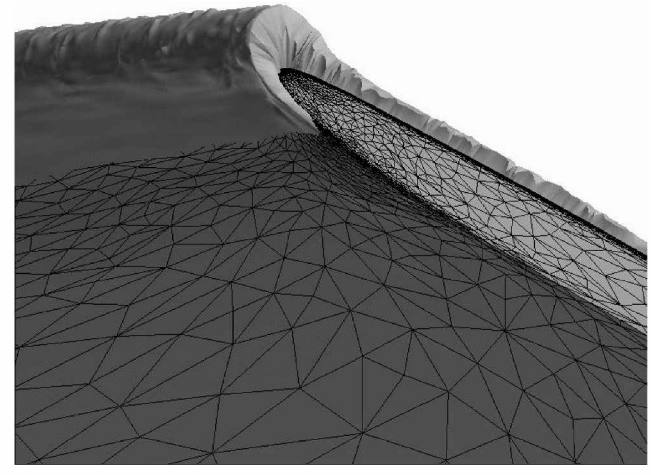

Fig. 17 Three-dimensional ice shape at blade tip.

on the upper side of the blade decreases from station 1 to station 4 (zone of positive Z in Fig. 16), showing a three-dimensional effect due to the negative twist angle.

Ice Accretion

Once the FENSAP airflow solution and the collection efficiency from DROP3D have been determined, ice accretion can be performed on the adapted grid. The 91-s exposure was simulated in one shot. The effect of intermediate airflow solutions with automatic mesh movement using the ALE package was not studied in this case because the inavailability of experimental data did not warrant the additional effort. Figure 17 gives a three-dimensional view of the ice accretion at the tip. The apparent roughness is due to the discrete representation of the surface by triangular faces.

Ice is assumed to grow in the direction normal to the wing surface. No correction is made on the node displacements to take into account the increase in area with the thickening of the ice. Usually, a tight coupling between the flow solver and the ice accretion module will insure that the volume of ice will correspond to the calculated ice mass divided by the ice density.

Two-dimensional cuts of the ice shape corresponding to stations 1–4 are plotted in Fig. 18. The global aspect of the ice shape qualitatively agrees with the numerical and experimental results of ONERA[6] (Fig. 19). However, no closer comparison can be made because of the discrepancies between the real geometry and the published one. In Fig. 19, we respect the scale published in Ref. 6. It

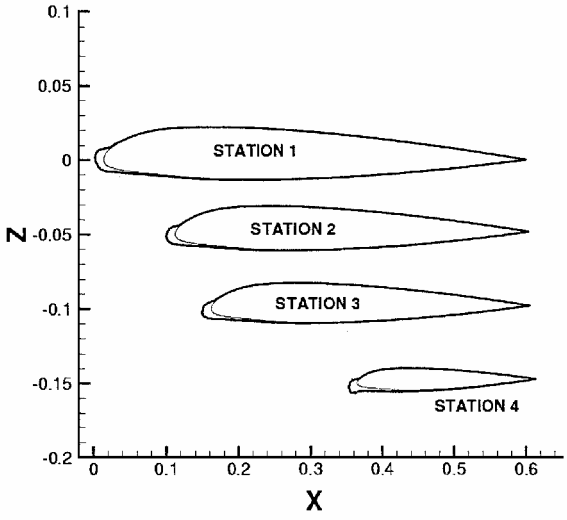

Fig. 18 Two-dimensional ice cuts along the spanwise direction for stations 1–4: ——, clean profile and ——, iced profile.

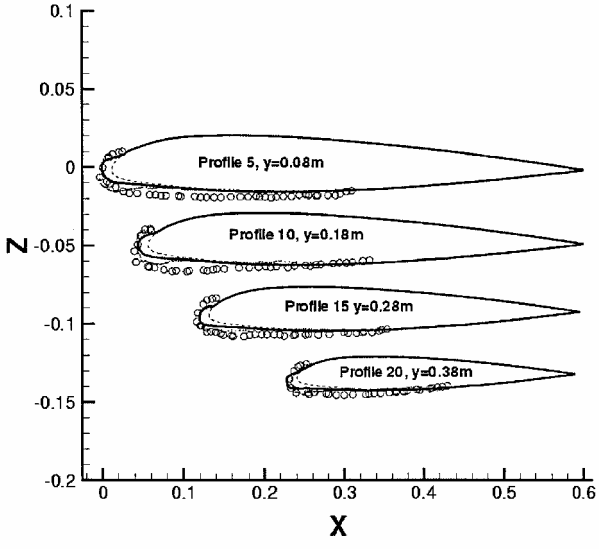

Fig. 19 Two-dimensional ice cuts along the spanwise direction; comparison between ICE3D and ONERA numerical solutions with the experimental solution: ○, experiments; . . . . , ONERA; - - - -, clean profile; and ——, ICE3D.

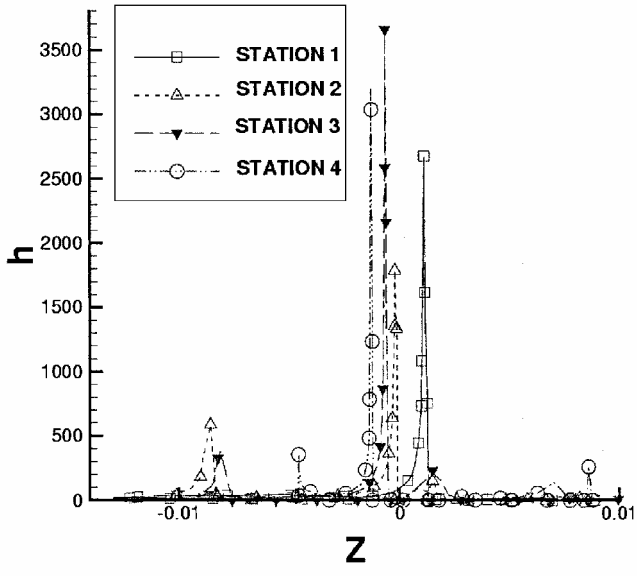

Fig. 20 Two-dimensional cuts of the modified convective heat transfer coefficient, in watts per square meter degrees Kelvin.

would have been interesting to compare with results from another two-dimensional icing code, but none of the existing codes was available for carrying out such a comparison. The three-dimensional effects are not spectacular because the geometry does not present strong three-dimensional features, and the very cold temperature corresponds to rime ice conditions, which makes water runback an unimportant factor.

Highlighting Three-Dimensional Capabilities of ICE3D

To highlight ICE3D's numerical three-dimensional capabilities, the convective heat flux has been modified (Fig. 20) to produce icing with runback, and the results of that study are presented in Figs. 21 and 22. The results may have no real physical meaning, but they show that the numerical method can predict three-dimensional icing with runback.

Two-dimensional cuts corresponding to stations 1–4 are also plotted in Fig. 22. The water runback in that case is quite important. The resulting ice shape is a lot more complex than the preceding one,

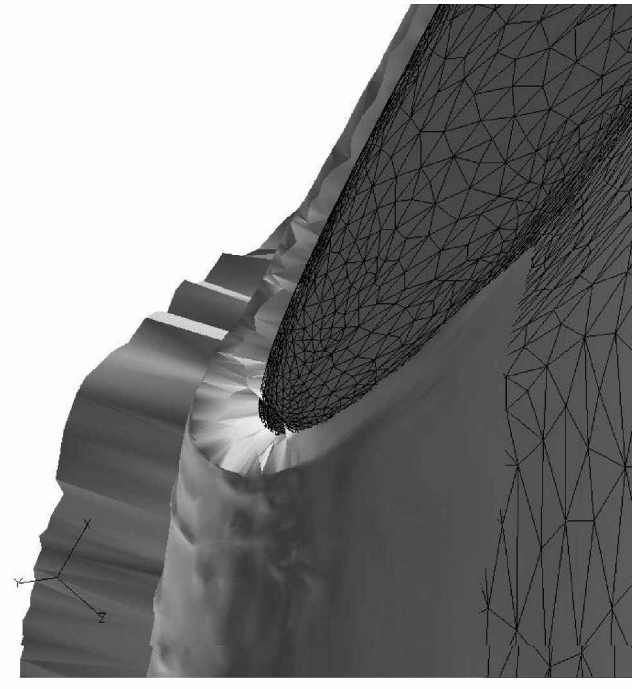

Fig. 21 Three-dimensional ice shape at blade tip.

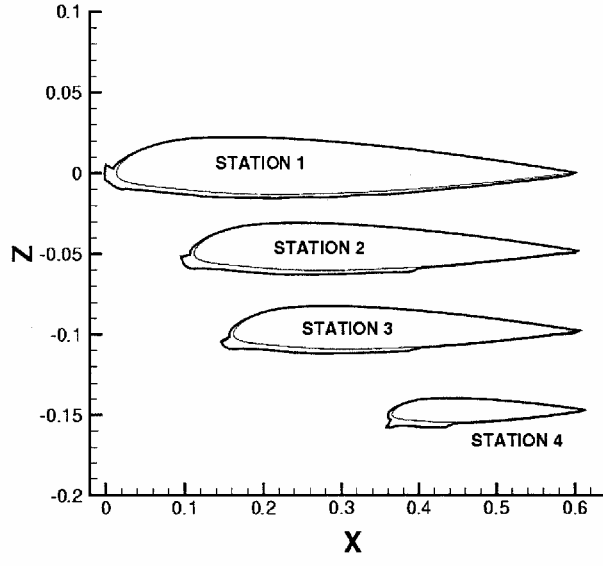

Fig. 22 Two-dimensional ice cuts along the spanwise direction for stations 1–4: ——, clean profile and ——, iced profile.

especially close to the tip, where the separation and tip vortex dramatically affect the ice accretion profile. It is also possible to observe drastically different spanwise behavior of the ice accretion process on a single geometry.

Conclusions

FENSAP-ICE has been shown to be a comprehensive icing system for in-flight ice simulations in three dimensions, as well as in two dimensions. It is built in a modular fashion with four modules (three described in this paper and the fourth, CHT3D, described in Ref. 5), each having a specific task but with all linked interactively. The airflow solution is computed with FENSAP or any other Euler or Navier–Stokes code. DROP3D uses the calculated airflow to compute droplet impingement without particle tracking. Finally, ICE3D computes the ice shape on the impacted surfaces using the shear stress and convective heat fluxes from the FENSAP solution and the water catch from DROP3D.

FENSAP-ICE has been shown to successfully predict collection efficiencies on two-dimensional and three-dimensional bodies. The interactive loop composed of the three modules has been used on structured, unstructured, and hybrid meshes, thus, providing great flexibility for being grafted to any CFD code.

The ice calculation module, ICE3D, has been partially validated in two dimensions and is in the final phases of its validation process in three dimensions, subject to the availability of appropriate data. It is almost as costly to run a two-dimensional test case as a three-dimensional one because the model and the method are three dimensional.

The validation process of ICE3D will continue in two and three dimensions. The influence of mesh density close to the leading edge and number of airflow solution updates on the ice shapes will be studied. Flexibility will be added to our flow solver by adding mesh adaptation tools to increase automatic mesh movement and eliminate the need for remeshing.

Antiicing capabilities will be developed inside the ice accretion module. For an imposed heat flux, ICE3D ought to be able to determine if any ice is forming on a given geometry.

References

[1]Hess, J. L., and Smith, A. M. O., "Calculation of Potential Flow About Arbitrary Bodies," *Progress in Aeronautical Sciences*, Vol. 8, Pergamon Press, 1967.

[2]Baruzzi, G. S., Habashi, W. G., Guèvremont, G., and Hafez, M. M., "A Second Order Finite Element Method for the Solution of the Transonic Euler and Navier–Stokes Equations," *International Journal for Numerical Methods in Fluids*, Vol. 20, No. 8, 1995, pp. 671–693.

[3]Bourgault, Y., Habashi, W. G., Dompierre, J., and Baruzzi, G. S., "A Finite Element Method Study of Eulerian Droplets Impingement Models," *International Journal for Numerical Methods in Fluids*, Vol. 29, No. 4, 1999, pp. 429–449.

[4]Beaugendre, H., Morency, F., and Habashi, W. G., "ICE3D, FENSAP-ICE's In-Flight Ice Accretion Module," *Proceeding of the 48th CASI Annual Conference*, Canadian Aeronautics and Space Inst., Toronto, 2001, pp. 271–276.

[5]Croce, G., Beaugendre, H., and Habashi, W. G., "CHT3D: FENSAP-ICE Conjugate Heat Transfer Computations with Droplet Impingement and Runback Effects," AIAA Paper 2002-0386, Jan. 2002.

[6]Hedde, T., and Guffond, D., "ONERA Three-Dimensional Icing Model," *AIAA Journal*, Vol. 33, No. 6, 1995, pp. 1038–1045.

[7]Spalart, P. R., and Allmaras, S. R., "A One-Equation Turbulence Model for Aerodynamic Flows," AIAA Paper 92-0439, Jan. 1992.

[8]Spalart, P. R., "Trends in Turbulence Treatments," AIAA Paper 2000-2306, Jan. 2000.

[9]Gresho, P. M., Lee, R. L., Sani, R. L., Maslanik, M. K., and Eaton, B. E., "The Consistent Galerkin FEM for Computing Derived Boundary Quantities in Thermal and/or Fluid Problems," *International Journal for Numerical Methods in Fluids*, Vol. 7, No. 4, 1987, pp. 371–394.

[10]Clift, R., Grace, J. R., and Weber, M. E., *Bubbles, Drops, and Particles*, Academic Press, New York, 1978, Chap. 5.

[11]Hughes, T. J. R., and Brooks, A., "A Theoretical Framework for Petrov–Galerkin Methods with Discontinuous Weighting Functions: Application to the Streamline-Upwind Procedure," *Finite Elements in Fluids*, Vol. 4, edited by R. H. Gallagher, D. H. Norrie, J. T. Oden and O. C. Zienkiewicz, Wiley, New York, 1982, Chap. 3.

[12]Messinger, B. L., "Equilibrium Temperature of an Unheated Icing Surface as a Function of Air Speed," *Journal of the Aeronautical Sciences*, Jan. 1953, pp. 29–42.

[13]Bourgault, Y., Beaugendre, H., and Habashi, W. G., "Development of a Shallow Water Icing Model in FENSAP-ICE," *Journal of Aircraft*, Vol. 37, No. 4, 2000, pp. 640–646.

[14]Morency, F., Tezok, F., and Paraschivoiu, I., "Anti-Icing System Simulation Using CANICE," *Journal of Aircraft*, Vol. 36, No. 6, 1999, pp. 999–1006.

[15]Cebeci, T., and Bradshaw, P., *Physical and Computational Aspects of Convective Heat Transfer*, Springer-Verlag, Berlin, 1984, pp. 72–82.

[16]Hedde, T., "Modélisation tridimensionnelle des dépôts de givre sur les voilures d'aéronefs," Ph.D. Dissertation, Univ. Blaise Pascal, Clermont–Ferrand II, 1992, Chap. 2.

[17]Ruff, G. A., and Berkowitz, M., "Users Manual for the NASA Lewis Ice Accretion Prediction Code (LEWICE)," NASA CR 185129, May 1990.

[18]Tran, P., Brahimi, M. T., and Paraschivoiu, I., "Ice Accretion on Aircraft Wings with Thermodynamic Effects," AIAA Paper 94-0605, Jan. 1994.

[19]Wright, W. B., and Rutkowski, A., "Validation Results for LEWICE 2.0" [CD-ROM], NASA CR 1999208690, Jan. 1999.

[20]Lepage, C. Y., Suerich-Gulick, F., and Habashi, W. G., "Anisotropic 3D Mesh Adaptation on Unstructured Hybrid Meshes," AIAA Paper 2002-0859, Jan. 2002.